Nanoscale

PAPER

View Article Online
View Journal | View Issue

Cite this: *Nanoscale*, 2018, **10**, 7465

Cooperative inter- and intra-layer lattice dynamics of photoexcited multi-walled carbon nanotubes studied by ultrafast electron diffraction†

Shuaishuai Sun, ‡[a] Zhongwen Li, ‡[a,b] Zi-An Li,[a] Ruijuan Xiao,[a] Ming Zhang,[a,b] Huanfang Tian,[a] Huaixin Yang[a,b] and Jianqi Li*[a,b,c]

Optical tuning and probing ultrafast structural response of nanomaterials driven by electronic excitation constitute a challenging but promising approach for understanding microscopic mechanisms and applications in microelectromechanical systems and optoelectrical devices. Here we use pulsed electron diffraction in a transmission electron microscope to investigate laser-induced tubular lattice dynamics of multi-walled carbon nanotubes (MWCNTs) with varying laser fluence and initial specimen temperature. Our photoexcitation experiments demonstrate cooperative and inverse collective atomic motions in intralayer and interlayer directions, whose strengths and rates depend on pump fluence. The electron-driven and thermally driven structural responses with opposite amplitudes cause a crossover between intralayer and interlayer directions. Our *ab initio* calculations support these findings and reveal that electrons excited from π to π* orbitals in a carbon tube weaken the intralayer bonds while strengthening the interlayer bonds along the radial direction. Moreover, by probing the structural dynamics of MWCNTs at initial temperatures of 300 and 100 K, we uncover the concomitance of thermal and nonthermal dynamical processes and their mutual influence in MWCNTs. Our results illustrate the nature of electron-driven nonthermal process and electron–phonon thermalization in the MWCNTs, and bear implications for the intricate energy conversion and transfer in materials at the nanoscale.

Received 16th January 2018,
Accepted 18th March 2018

DOI: 10.1039/c8nr00432c

rsc.li/nanoscale

Introduction

Novel nanostructured materials with fast electronic responses are currently actively pursued for building miniaturized optoelectronic devices with high-speed circuitry performance. The candidate materials are one-dimensional (1D) carbon nanotubes (CNTs)[1–3] and two-dimensional (2D) graphene and transition metal dichalcogenides (TMDCs).[4–9] A detailed microscopic understanding of their ultrafast carrier relaxation and lattice dynamics is the key for designing and engineering novel carbon-based optoelectronic devices.[10] Ultrafast optical spectroscopy techniques[11,12] have been extensively used to study carbon-based materials and provided crucial information about their electronic dynamics.[13,14] However, due to the insensitivity of optical spectroscopy to structural changes, the direct information of lattice response after laser excitation is largely inaccessible, which is crucial for application in microelectromechanical systems (MEMS). Studying the ultrafast structural dynamics requires not only sufficient time resolution but also efficient means for atomic structure determination. Ultrafast X-ray diffraction (UXRD)[15–17] and ultrafast electron diffraction (UED)[16,18] provide a direct access to lattice dynamics with high spatiotemporal resolution and give insights into the thermally/carrier-driven atomic structural dynamics in femtosecond to picosecond time scales. Probing ultrafast structural response induced by electronic excitation, *i.e.* a nonthermal effect, is generally considered to be a great challenge due to the process being very fast with very small amplitudes of lattice response. With modest excitation below the melting threshold in UED experiments, a carrier-induced lattice contraction followed by a large thermal expansion was reported in the interlayer direction of graphite.[19,20] At low excitation densities in UXRD experiments, the above band-gap optical excitation in the TMDCs leads to an unexpected large-amplitude, ultrafast contraction between the two-dimensional layers arising from a dynamic modulation of the interlayer van

[a]*Beijing National Laboratory for Condensed Matter Physics, Institute of Physics, Chinese Academy of Sciences, Beijing 100190, China. E-mail: ljq@aphy.iphy.ac.cn*
[b]*School of Physical Sciences, University of Chinese Academy of Sciences, Beijing 100049, China*
[c]*Collaborative Innovation Centre of Quantum Matter, Beijing 100084, China*
†Electronic supplementary information (ESI) available: Full cycle of ultrafast structural dynamics; pump laser fluence dependence of structural dynamics; TEM lattice images taken after pump laser irradiation. See DOI: 10.1039/c8nr00432c
‡These authors contributed equally to this work.

der Waals interactions.[9] A recent report[21] has revealed the reversible structural dynamics of multi-walled carbon nanotubes (MWCNTs) involving a striking electron-driven lattice expansion along the axial direction. We note that in ref. 21 the nonthermal lattice responses are only observed in the axial direction (covalent bonds within the carbon intralayer) for a single laser fluence, while the nonthermal effect in the radial direction (van der Waals bonds in the carbon interlayer) is absent. Moreover, the observed nonthermal axial expansion time constant is ~1.3 ps and then the recovery of the axial lattice takes about 17 ps. In this time span, the thermal process of hot electrons thermalizing phonons is expected to occur concurrently, that is, the nonthermal atomic motions are inevitably affected by the thermal process *via* electron–phonon scattering.

In this article, UED techniques are used to follow both the radial and axial responses of MWCNTs upon laser excitation. We find that nonthermal atomic motions in MWCNTs result in rapid intralayer expansions and interlayer contractions. The cooperative and inverse collective atomic motion in intralayer and interlayer directions provides a true time-resolved three-dimensional (3D) visualization of electron-driven atomic motions and gives insights into the characteristics of nonthermal lattice response in highly anisotropic structures. By probing the lattice dynamics of specimens at different initial specimen temperatures (300 and 100 K), we observe a dramatic difference in lattice responses for the two temperatures used, and explain the underlying physics as being the concurrence and mutual influence of thermal and nonthermal processes in the highly anisotropic CNT system. Our results should contribute to the understanding of ultrafast electronic and atomic dynamics in MWCNTs that could lead to efficient ways of control of both electron and atom degrees of freedom for ultrafast device applications.

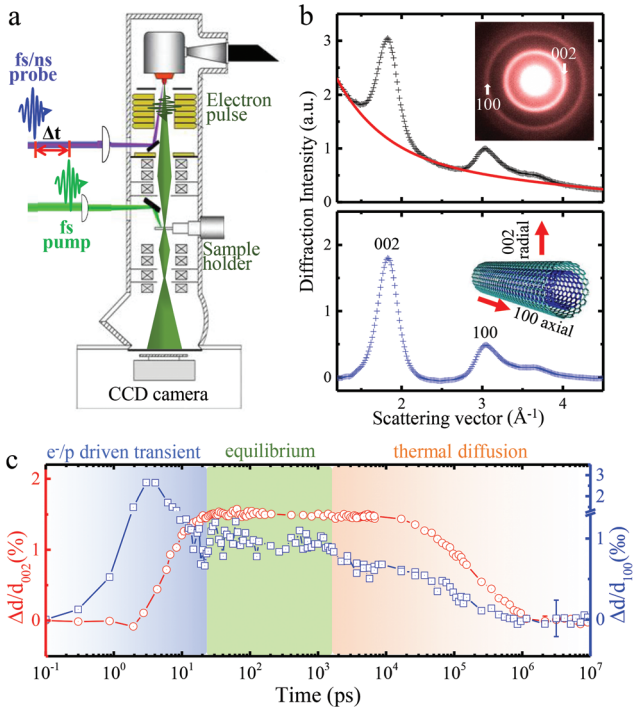

Fig. 1 Schematic illustration of ultrafast transmission electron microscopy (UTEM) and reversible ultrafast structural dynamics of multi-walled carbon nanotubes (MWCNTs). (a) Pump–probe scheme in the UTEM. The pump laser (520 nm wavelength, 300 fs duration) initiates the ultrafast process and sets the time as zero. A second probe laser (347 nm wavelength, 300 fs duration or 355 nm wavelength, 10 ns duration) is used to generate pulsed electrons for taking diffraction patterns with time Δt. (b) Transient 1D electron diffraction profiles radially integrated from a 2D diffraction pattern. The upper panel shows the as-obtained diffraction profile and the baseline (red curve). The lower panel shows the baseline-subtracted diffraction profile. The insets in (b) are the typical pulsed electron diffraction pattern and atomic model of MWCNTs with the radial and axial directions and crystallographic planes of (002) and (100) indicated. (c) A temporal phase diagram of the reversible structural evolution of photoexcited MWCNTs for a fluence of 45 mJ cm^{-2}.

Materials and methods

Source of MWCNTs and TEM specimen preparation

The MWCNT samples used here were synthesized by catalytic cracking of natural gas (Chengdu Organic Chemicals Co. Ltd), which are a mixed type comprised of both metallic and semiconducting ones. For UED experiments, MWCNTs were dispersed in ethanol using an ultrasonicator, and a few droplets of a suspension were cast onto a 2000-mesh copper grid. A second 400-mesh copper grid was placed on top of the 2000-mesh grid to sandwich the specimens to enhance their mechanical stability during laser excitation. As a result, the specimen consisted of a woven porous network of randomly oriented nanotubes. The MWCNT samples have an average diameter of 40 ± 10 nm and typical lengths of 10–20 μm.

UTEM instrument and experiment

The UED experiments of MWCNTs were performed using our home-built ultrafast transmission electron microscope (UTEM) modified from a JEOL-2000EX microscope, as shown schematically in Fig. 1a. The electron gun was operated at 160 kV with a LaB_6 photocathode, driven by 300 fs laser pulses (347 nm) or 10 ns laser pulses (355 nm) at suitable repetition rates in the femtosecond (fs) or nanosecond (ns) stroboscopic imaging mode, respectively. The photo-induced structural dynamics was initiated by a second 300 fs pump laser (520 nm) with a variable fluence of up to 120 mJ cm^{-2}. The laser spot at the sample has a size of about 100 μm ($1/e^2$ of the peak intensity). The electron beam was spread uniformly to around 20 μm and a collection of randomly oriented tubes with 5 μm diameter by a selected area aperture were used for electron diffraction. Time-resolved electron diffraction patterns were recorded using a charge coupled device (CCD) camera with an exposure time of 10 seconds for each diffraction pattern. The overall temporal resolution for the femtosecond stroboscopic mode was found to be about 1 picosecond. More details about the characteristics and the performance of our UTEM have been previously reported.[22–25]

Analysis of ultrafast electron diffraction

A typical 2D diffraction pattern of MWCNTs (inset in Fig. 1b) is radially integrated into a 1D diffraction profile, as shown in Fig. 1b, in which the upper panel is the as-obtained diffraction profile and the lower panel is the one after baseline (red curve) subtraction. The diffraction baseline was fitted with a three-exponential function and subtracted from the as-obtained 1D diffraction profile. The change in lattice spacing, $\Delta d/d = -\Delta R/R$, can be deduced using the formula $Rd = L\lambda$, in which R is the radius of the diffraction ring, d is the lattice spacing, L is the camera length, and λ is the de Broglie wavelength of electrons. The measurement precision for the lattice change by evaluating the peak shift of the diffraction profile was estimated to be 0.25‰. The inset of Fig. 1b depicts the tubular structure of MWCNTs with two distinct chemical bonds, *i.e.*, the strong covalent bonds within the (100) intralayer, and the weak van der Waals bonds within the (002) interlayer.

Results and discussion

Structural dynamics of photoexcited MWCNTs in a reversible cycle

To be assured that the structural dynamics of MWCNTs is reversible for stroboscopic observation, we first monitor the structural responses of photoexcited MWCNTs at a long time delay of up to 100 μs at 10 kHz repetition rates within the fs and ns stroboscopic imaging mode. Fig. 1c shows the temporal changes of interlayer spaces ($\Delta d/d_{002}$) and intralayer spaces ($\Delta d/d_{100}$) of MWCNTs for a fluence of 45 mJ cm^{-2}, illustrating a full cycle of structural dynamics with distinct sequences: rapid electron–phonon driven transient process at an early time, then a new thermal quasi-equilibrated state, and a relatively slow thermodiffusion process at a longer time. In the full cycle, the MWCNTs exhibit a strong anisotropic behavior of lattice dynamics due to their distinct chemical bonding. The time span for such a full dynamical cycle is determined to be ~1 μs in the MWCNTs (Fig. S1 in the ESI†), which is determined by the thermal diffusion process of materials and heat transport between the materials and the supports. Therefore, we set the repetition rate of the pump laser to be 100 kHz (*i.e.* the pulse repetition *interval* of 10 μs) to ensure reversible processes for stroboscopic observation in the following study.

Cooperative radial contraction and axial expansion in MWCNTs driven by electronic excitation: experimental observation

Fig. 2a shows the temporal evolution of the lattice spacings for the (002) and (100) planes. At longer time delays (>30 ps) both the radial and axial directions expand as the hot carriers thermalizing the lattice. One can estimate the temperature rise ΔT to be ~500 K using the thermal expansion coefficient[26,27] α_{002} = ~3 × 10^{-5} K^{-1} and the radial (002) spacing expansion of 1.5% at 30 ps. Strikingly, at an early time t < 5 ps the axial (100) spacings exhibit a rapid expansion and then a partial recovery; in contrast, the radial (002) spacings exhibit a rapid contraction, followed by a thermal phonon-driven large amplitude expansion. The thermal response caused by the electron–phonon coupling process predicted using the two-temperature model is demonstrated as a single exponential process. In order to quantify the nonthermal process, we subtract the thermal phonon-driven component (approximated by an exponential function with a time constant of 5 ps) from the total lattice changes (Fig. 2a) to yield the nonthermal electron-driven component (Fig. 2b). For the evolution of the lattice spacing along the axial direction, it can be fitted with the combination of a fast exponential increase with a time constant of 1 ± 0.5 ps and a slow exponential decay of 4 ± 1 ps, as discussed previously.[21] Similarly, the dynamical changes of the interlayer spacing along the radial direction can be characterized by a fast exponential decrease and a slow exponential expansion with the same time constants as for the axial direction. The time for reaching the maximal nonthermal effect of both the axial and the radial directions is estimated to be ~3 ps. The experimentally observed nonthermal lattice dynamics of both the radial and axial directions in MWCNTs, as driven by electronic excitation, demonstrate cooperative and inverse collective atomic motions and provide a four-dimensional (4D) view of atomic motions at the nanoscale.

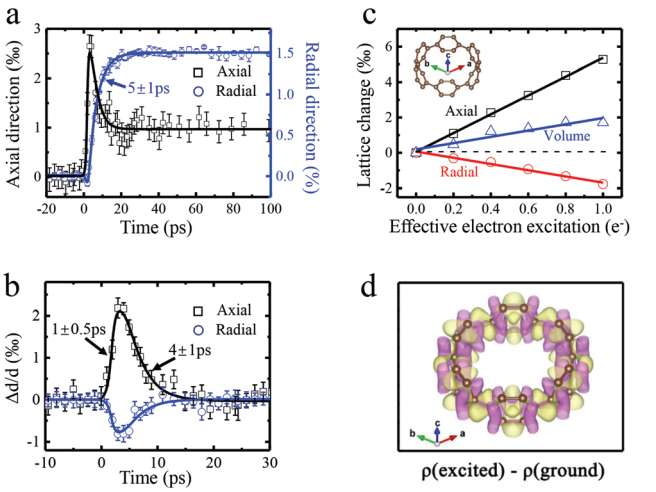

Fig. 2 Experimental and theoretical investigations of ultrafast structural changes of MWCNTs upon pulsed fs-laser excitation. (a) Time-resolved structural changes as obtained from UED with a fluence of 45 mJ cm^{-2}, illustrating nonthermal lattice motions in both the axial and radial directions. (b) The nonthermal components extracted from (a) after the subtraction of the thermal contribution (a single-exponential with a time constant of 5 ps) to the total lattice change. The nonthermal responses are fitted with a fast exponential response (1 ± 0.5 ps) and a slow exponential decay (4 ± 1 ps). (c) Calculated lattice changes for a single-walled carbon nanotube as a function of effective electron excitation, illustrating the essential different features driven by π to π* excitation. The inset shows the atomic model of a single-walled carbon nanotube. (d) Alteration of the electron density between the ground and excited states (following electron excitation from π to π*). The charge density decreases in the axial direction (yellow isosurfaces) and increases in the C–C bonds along the radial direction (purple isosurfaces).

Theoretical verification

In order to understand the lattice dynamics driven by the photoexcited electrons, we performed an extensive investigation on the effects of the laser pulse on the electronic structure and chemical bonding in a carbon nanotube using *ab initio* DFT calculations. The Vienna *ab initio* simulation package (VASP)[28] for the projector augmented-wave (PAW) approach[29] was adopted for our DFT calculations. The exchange–correlation function is described using the generalized gradient approximation in the parameterization of the Perdew, Burke, and Ernzerhof (PBE) functional.[30] The cut-offs of wave function and charge density are 600 and 900 eV, respectively. The single-walled carbon nanotube, as used for the theoretical analysis of intralayer atom motions, is modelled using a unit cell with 24 carbon atoms in a 19.889 × 19.889 × 2.465 Å^3 hexagonal lattice, where sufficient vacuum is introduced around the nanotube to avoid interactions among neighboring images because of the translational periodicity (see the inset of Fig. 2c). In this model, the unit cells are fully optimized using a *k*-mesh with a density of one point per ~0.03 Å^{-3} to obtain the change of the nanotube along the axial and radial directions caused by electronic excitation. For the relaxation of all the cases, the forces exerted by each of the atoms are well converged below 0.01 eV Å^{-1}, and the total energies are converged below 10^{-5} eV per cell.

The electronic structures of MWCNTs consist of a σ band with a very large bandgap and a π band around the Fermi level. Hence, the optical excitation at 520 nm (2.4 eV) promotes electrons from the π to the π* states. The photoexcitation effect is simulated by a fixed partial electron occupancy, *i.e.*, a fraction of electrons from the highest occupied state are moved to the lowest unoccupied state. Fig. 2c depicts the changes in lattice spacings of the carbon nanotube as a function of excited electrons, in which upon increasing the excitation level, the axial expansion (black squares) and radial contraction (red circles) are clearly revealed. At the excitation level of one electron (from π to π* orbitals), the axial direction of the nanotube expands by about 5.3‰, while the radial direction shrinks by 1.8‰. It is also informative to show the changes in the unit-cell volume as a function of the excitation level (blue triangles in Fig. 2c).

Fig. 2d shows the charge density ρ difference between the ground and excited states for a single-walled carbon nanotube, in which the charge densities of π-bonds on carbon rings decrease (purple isosurfaces), while those of the σ-bonds (yellow isosurfaces) increase. The charge density changes upon electronic excitation for the two types of bonds exhibit an opposite behavior of charge redistribution. The depopulation of electrons (in the band picture from π bands to unoccupied π* bands) in the π-bond upon laser excitation weakens the intralayer C–C bonds, which explains the expansion in the (100) axial direction observed in experiments. On the other hand, the gain in the charge density of the σ-bond perpendicular to the axial direction strengthens the interlayer interaction and shortens the interlayer spacing, in accordance with the experimentally observed radial contraction of MWCNTs upon photoexcitation.

Laser fluence dependence of the nonthermal process in MWCNTs

We now proceed to study the fluence-dependent structural dynamics of MWCNTs. At an early time (t < 5 ps), the magnitudes of both the radial contractions (Fig. 3a) and of the axial expansions (Fig. 3b) depend strongly on the applied pump laser fluence: a trend that a higher fluence leads to enhanced nonthermal lattice changes. It is noteworthy that the magnitude of nonthermal response along the (100) axial direction is much larger than that along the (002) radial direction, which is supported by our *ab initio* calculations (Fig. 2c). Fig. 3c plots the fluence-dependent maxima of nonthermal radial contractions in Fig. 3a and axial expansions in Fig. 3b, to illustrate the nature of nonthermal transient lattice changes driven by electronic excitation. The features of electron-driven radial contraction and axial expansion of MWCNTs are essentially correlated with the highly anisotropic electronic bonds in the tubular structure, *i.e.*, the interlayer van de Waals bonds and the intralayer covalent bonds. Note that while the electron-driven axial expansion exhibits a nearly monotonic behavior with respect to the applied fluence of up to 45 mJ cm^{-2}, the fluence-dependent radial contractions show a nonlinear feature with threshold-switching effects, as also seen clearly in Fig. S2d in the ESI.†

At a relatively long time (t > 20 ps), at which hot electrons thermalize phonons to a new thermal equilibrium state (Fig. S2a and S2b in the ESI†), the thermal phonon-driven lattice expansion in the new thermal state also exhibits a

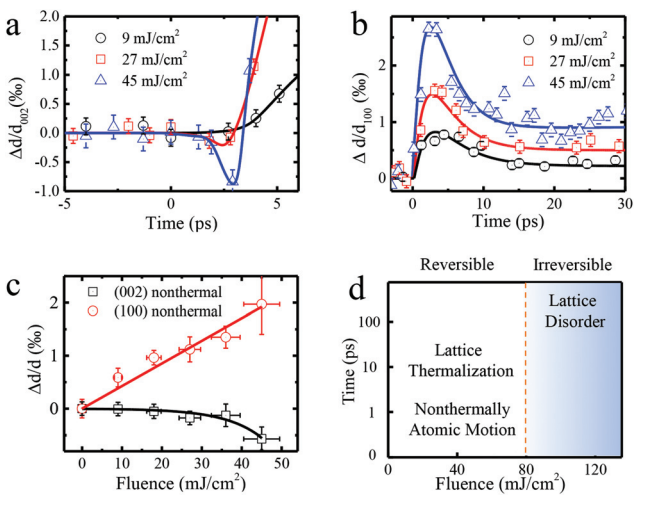

Fig. 3 The fluence dependence of nonthermal structural changes of MWCNTs. (a, b) Transient evolution of the peak position for the radial (002) plane and for the axial (100) plane, respectively. (c) Fluence dependence of the maximal nonthermal response for the (002) and (100) planes taken at a time delay of 3 ps. The solid lines are guide to the eyes. (d) Regime diagram summarizes the timescale and fluence dependence of structural changes of MWCNTs upon femtosecond laser pulse excitation. Laser fluence ranges from 0 to 120 mJ cm^{-2}.

linear response depending on the pump fluence (Fig. S2c in the ESI†). We also performed experiments with a higher laser fluence up to 120 mJ cm^{-2} to determine the threshold fluence above which the irreversible lattice changes occur. Fig. 3d summarizes the fluence dependence of the lattice dynamics of MWCNTs with a determined fluence threshold of ~80 mJ cm^{-2}, above which lattice defects and damage of the tubular structure set in, as shown in Fig. S3 in the ESI,† and below which, the MWCNTs undergo reversible dynamical processes involving rapid nonthermal responses and electron–phonon thermalization.

Effects of initial specimen temperature on the nonthermal and thermal responses

Our ultrafast studies on MWCNTs described above and the results of a previous report[21] clearly show that subsequent to photoexcitation the rapid increase of nonthermal lattice responses (around 1 or 2 picoseconds) of MWCNTs are followed by a relatively slow (tens of picoseconds) nonthermal lattice relaxation. Consequently, thermal processes *via* electron–phonon scattering are expected to occur alongside with the recovery of nonthermal effects. In order to study the entangled nonthermal and thermal processes in MWCNTs, we designed ultrafast experiments using an *in situ* cooling holder to provide different initial specimen temperatures. Fig. 4a and b show the respective temporal evolution of (002) interlayer and (100) intralayer spacings for two initial specimen temperatures of 300 and 100 K. In Fig. 4a, the radial expansions at 300 K exhibit a faster electron–phonon thermalization than that at 100 K, as evidenced by their respective estimated time constants of τ = 5 ± 1 ps for 300 K and τ = 11 ± 2 ps for 100 K. We attribute these different thermalization rates to the temperature-dependent phonon density of the specimen. Qualitatively, the lower the specimen temperature the lower the occupied phonon density, resulting in longer time needed for electron–phonon thermalization, as previously discussed.[31–33] It should be noted that at a longer time (t > 40 ps) of a new thermal equilibrium, the magnitudes of radial expansion for both cases of 300 K and 100 K are nearly identical.

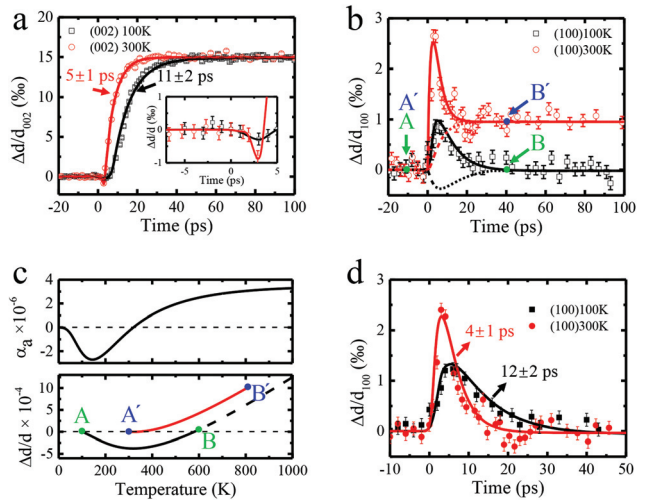

Fig. 4 Influence of initial specimen temperature on the lattice dynamics of MWCNTs. (a, b) Radial (002)- and axial (100)-lattice dynamics upon pulsed laser excitation with a fluence of 45 mJ cm^{-2} obtained at initial temperatures of 300 K and 100 K, respectively. The inset in (a) shows an enlarged region at the early time. (c) The upper panel displays the intralayer coefficient of thermal expansion (CTE, α_a) of a MWCNT, showing the negative intralayer CTE at a relatively low-temperature range. The lower panel displays the lattice response after a temperature rise of ΔT = 500 K from the initial specimen temperatures of 100 K (black curve A–B) and 300 K (red curve A′–B′), respectively. (d) The nonthermal components extracted from (b) after the subtraction of the thermally driven contribution (dashed curves in (b)) to the lattice change, illustrating visibly different motions for the initial temperatures of 100 K and 300 K. The axial nonthermal recovery processes are fitted by an exponential function with the time constants as indicated.

In Fig. 4b, the axial lattice responses of MWCNTs at initial temperatures of 300 and 100 K present two prominent features: (a) the magnitude of axial thermal expansion (t > 40 ps) for 300 K (~1‰) is much larger than that for 100 K (almost zero); and (b) the magnitude of axial nonthermal expansion for 300 K is larger than that for 100 K. The first feature of the axial responses is in stark contrast to the nearly identical thermal expansions of the radial response for both specimen temperatures (see Fig. 4a). To better understand this striking feature, we invoke the strong temperature-dependent coefficient of thermal expansion (CTE) for carbon-based materials, such as graphite[34–39] and nanotube.[39–42] Fig. 4c plots the axial CTE $\alpha_a(T)$ adopted from ref. 35 and the calculated relative axial changes $\Delta d/d_{100}$ for 300 and 100 K. Interestingly, the negative CTE for $\alpha_a(T)$ in the low temperature range (<300 K) leads to lattice contraction as the specimen temperature rises. Using the $\alpha_a(T)$ and the measured lattice temperature rise of ΔT = 500 K (see the above text related to Fig. 2a), one can calculate the radial thermal changes for initial specimen temperatures (Fig. 4c) of 300 K (red curve marked by A′–B′) and 100 K (black curve marked by A–B). It is now clear that the first feature of different magnitudes of axial thermal expansion for different initial specimen temperatures is associated with the peculiar negative part of the axial $\alpha_a(T)$, while the radial $\alpha_c(T)$ (not shown here) is also temperature-dependent but always has positive values.[35]

Owing to the fact that the occurrence of nonthermal and thermal processes, especially the nonthermal recovery at tens of picoseconds, it should be ideal to separate the two contributions for their respective quantification. In such attempts, the axial thermal parts for 300 and 100 K (their respective red and black dashed curves in Fig. 4b) are calculated using the formula $\Delta d(t)/d_0 = \int_{T_0}^{T(t)} \alpha_a(T)\mathrm{d}T$, where $T(t) = \Delta T(1 - \exp(-t/\tau)) + T_0$, and τ is the time constant of electron–phonon thermalization estimated from Fig. 4a. Fig. 4d shows the axial nonthermal parts subtracted from the thermal parts, in which the 300 K case shows a higher radial nonthermal expansion than the 100 K case. Moreover, the rates of increase and recovery of the axial nonthermal responses for 300 K are also faster than those for 100 K. It is also noted that for both temperatures, their respective time constants for the increase of thermal

expansion in the radial direction are similar to those for the nonthermal recovery in the axial direction, as evidenced in the estimated time constants indicated in Fig. 4a and d. This suggests that the nonthermal electron-driven lattice recovery process is concomitant with the thermal carrier–phonon relaxation. The magnitude of the nonthermal lattice response depending on the initial specimen temperature could be associated with the temperature dependence of energy gap and intraband carrier scattering in solids.[12] Future ultrafast experiments and theoretical analysis should address quantitatively the lattice dynamics of solids involving intricate entanglement of electron-driven nonthermal and phonon-driven thermal processes.

Conclusions

In the present study, we used the pulsed electron diffraction in UTEM to follow the nonthermal lattice dynamics of MWCNTs in the picosecond time scale with the ability of direct transient structure determination. Our results reveal the nonthermal nature of both the radial contraction and the axial expansion in the MWCNTs upon photoexcitation, thus demonstrating a 4D visualization of electron-driven cooperative atomic motions in intralayer and interlayer directions, supported by *ab initio* calculations. By probing the structural dynamics of MWCNTs at initial temperatures of 300 and 100 K, we uncover the concomitance of thermal and nonthermal dynamical processes and their mutual influence in MWCNTs. Our ultrafast exploration is expected to be applicable for other highly anisotropic 2D materials and layered compounds. From the methodological perspective, the present studies demonstrate that owing to the large matter-electron scattering cross-sections, the direct access to atomic structures, and the less-scale facility of even table-top apparatus, pulsed electron diffraction and microscopy in the UTEM with fs/ns stroboscopic mode are powerful tools to obtain a complete temporal phase diagram of the ultrafast structural dynamics of nanomaterials and the associated energy transfer at the nanoscale.

Conflicts of interest

There are no conflicts to declare.

Acknowledgements

This work was supported by the National Basic Research Program of China 973 Program (No. 2015CB921300), the National Key Research and Development Program of China (No. 2016YFA0300300, 2017YFA0303000, 2017YFA0504703, and 2017YFA0302904), the Natural Science Foundation of China (No. 11447703, 11604372, 11474323, 11774403 and 11774391), "Strategic Priority Research Program (B)" of the Chinese Academy of Sciences (No. XDB07020000), and the Scientific Instrument Developing Project of the Chinese Academy of Sciences (No. ZDKYYQ20170002). Z.-A. L acknowledges the Hundred Talent Program B of Chinese Academy of Sciences.

Notes and references

1 S. Tatsuura, M. Furuki, Y. Sato, I. Iwasa, M. Tian and H. Mitsu, *Adv. Mater.*, 2003, **15**, 534–537.
2 C. Klinke, J. B. Hannon, A. Afzali and P. Avouris, *Nano Lett.*, 2006, **6**, 906–910.
3 C. Li, X. Zhou, F. Zhai, Z. Li, F. Yao, R. Qiao, K. Chen, M. T. Cole, D. Yu, Z. Sun, K. Liu and Q. Dai, *Adv. Mater.*, 2017, **29**, 1701580.
4 D. Jariwala, V. K. Sangwan, L. J. Lauhon, T. J. Marks and M. C. Hersam, *ACS Nano*, 2014, **8**, 1102–1120.
5 Q. H. Wang, K. Kalantar-Zadeh, A. Kis, J. N. Coleman and M. S. Strano, *Nat. Nanotechnol.*, 2012, **7**, 699–712.
6 E. M. Mannebach, R. Li, K. A. Duerloo, C. Nyby, P. Zalden, T. Vecchione, F. Ernst, A. H. Reid, T. Chase, X. Shen, S. Weathersby, C. Hast, R. Hettel, R. Coffee, N. Hartmann, A. R. Fry, Y. Yu, L. Cao, T. F. Heinz, E. J. Reed, H. A. Dürr, X. Wang and A. M. Lindenberg, *Nano Lett.*, 2015, **15**, 6889–6895.
7 M. F. Lin, V. Kochat, A. Krishnamoorthy, L. Bassman, C. Weninger, Q. Zheng, X. Zhang, A. Apte, C. S. Tiwary, X. Shen, R. Li, R. Kalia, P. Ajayan, A. Nakano, P. Vashishta, F. Shimojo, X. Wang, D. M. Fritz and U. Bergmann, *Nat. Commun.*, 2017, **8**, 1–8.
8 C. Ruppert, A. Chernikov, H. M. Hill, A. F. Rigosi and T. F. Heinz, *Nano Lett.*, 2017, **17**, 644–651.
9 E. M. Mannebach, C. Nyby, F. Ernst, Y. Zhou, J. Tolsma, Y. Li, M.-J. Sher, I.-C. Tung, H. Zhou, Q. Zhang, K. Seyler, G. Clark, Y. Lin, D. Zhu, J. M. Glownia, M. E. Kozina, S. Song, S. Nelson, A. Mehta, Y. Yu, A. Pant, O. B. Aslan, A. Raja, Y. Guo, A. DiChiara, W. L. Mao, L. Cao, S. Tongay, J. Sun, D. J. Singh, T. F. Heinz, X. Xu, A. H. MacDonald, E. J. Reed, H. Wen and A. M. Lindenberg, *Nano Lett.*, 2017, **17**, 7761–7766.
10 P. Avouris, Z. Chen and V. Perebeinos, *Nat. Nanotechnol.*, 2007, **2**, 605–615.
11 A. Othonos, *J. Appl. Phys.*, 1998, **83**, 1789–1830.
12 S. K. Sundaram and E. Mazur, *Nat. Mater.*, 2002, **1**, 217–224.
13 F. Wang, G. Dukovic, L. E. Brus and T. F. Heinz, *Phys. Rev. Lett.*, 2004, **92**, 17–20.
14 G. N. Ostojic, S. Zaric, J. Kono, M. S. Strano, V. C. Moore, R. H. Hauge and R. E. Smalley, *Phys. Rev. Lett.*, 2004, **92**, 1–4.
15 M. Bargheer, N. Zhavoronkov, M. Woerner and T. Elsaesser, *ChemPhysChem*, 2006, **7**, 783–792.
16 M. Chergui and A. H. Zewail, *ChemPhysChem*, 2009, **10**, 28–43.
17 A. M. Lindenberg, S. L. Johnson and D. A. Reis, *Annu. Rev. Mater. Res.*, 2017, **47**, 425–449.
18 G. Sciaini and R. J. D. Miller, *Rep. Prog. Phys.*, 2011, **74**, 96101.

19 F. Carbone, P. Baum, P. Rudolf and A. H. Zewail, *Phys. Rev. Lett.*, 2008, **100**, 35501.
20 R. K. Raman, Y. Murooka, C.-Y. Ruan, T. Yang, S. Berber and D. Tománek, *Phys. Rev. Lett.*, 2008, **101**, 77401.
21 G. M. Vanacore, R. M. Van Der Veen and A. H. Zewail, *ACS Nano*, 2015, **9**, 1721–1729.
22 L. Wei, S. Sun, C. Guo, Z. Li, K. Sun, Y. Liu, W. Lu, Y. Sun, H. Tian, H. Yang and J. Li, *Struct. Dyn.*, 2017, **4**, 44012.
23 Z. Li, S. Sun, Z.-A. Li, M. Zhang, G. Cao, H. Tian, H. Yang and J. Li, *Nanoscale*, 2017, **9**, 13313–13319.
24 S. Sun, L. Wei, Z. Li, G. Cao, Y. Liu, W. J. Lu, Y. P. Sun, H. Tian, H. Yang and J. Li, *Phys. Rev. B: Condens. Matter*, 2015, **92**, 224303.
25 G. Cao, S. Sun, Z. Li, H. Tian, H. Yang and J. Li, *Sci. Rep.*, 2015, **5**, 8404.
26 S. Bandow, *J. Appl. Phys.*, 1997, **36**, L1403–L1405.
27 Y. Maniwa, R. Fujiwara, H. Kira, H. Tou, E. Nishibori, M. Takata, M. Sakata, A. Fujiwara, X. Zhao, S. Iijima and Y. Ando, *Phys. Rev. B: Condens. Matter*, 2001, **64**, 73105.
28 P. E. Blöchl, *Phys. Rev. B: Condens. Matter*, 1994, **50**, 17953–17979.
29 G. Kresse and J. Furthmüller, *Comput. Mater. Sci.*, 1996, **6**, 15–50.
30 J. P. Perdew, K. Burke and M. Ernzerhof, *Phys. Rev. Lett.*, 1996, **77**, 3865–3868.
31 I. Chatzakis, H. Yan, D. Song, S. Berciaud and T. F. Heinz, *Phys. Rev. B: Condens. Matter*, 2011, **83**, 205411.
32 M. Scheuch, T. Kampfrath, M. Wolf, K. Von Volkmann, C. Frischkorn and L. Perfetti, *Appl. Phys. Lett.*, 2011, **99**, 2011–2014.
33 K. T. Tsen and D. K. Ferry, *J. Phys.: Condens. Matter*, 2009, **21**, 174202.
34 A. C. Bailey and B. Yates, *J. Appl. Phys.*, 1970, **41**, 5088–5091.
35 D. K. L. Tsang, B. J. Marsden, S. L. Fok and G. Hall, *Carbon*, 2005, **43**, 2902–2906.
36 W. Bao, F. Miao, Z. Chen, H. Zhang, W. Jang, C. Dames and C. N. Lau, *Nat. Nanotechnol.*, 2009, **4**, 562–566.
37 N. Mounet and N. Marzari, *Phys. Rev. B: Condens. Matter*, 2005, **71**, 205214.
38 A. E. Mag-isa, J. Kim and C. Oh, *Mater. Lett.*, 2016, **171**, 312–314.
39 J.-W. Jiang, J.-S. Wang and B. Li, *Phys. Rev. B: Condens. Matter*, 2009, **80**, 205429.
40 Y.-K. Kwon, S. Berber and D. Tománek, *Phys. Rev. Lett.*, 2004, **92**, 15901.
41 K. Shirasu, G. Yamamoto, I. Tamaki, T. Ogasawara, Y. Shimamura, Y. Inoue and T. Hashida, *Carbon.*, 2015, **95**, 904–909.
42 H. Jiang, B. Liu, Y. Huang and K. C. Hwang, *J. Eng. Mater. Technol.*, 2004, **126**, 265.